Multifrequency AFM reveals lipid membrane mechanical properties and the effect of cholesterol in modulating viscoelasticity

Classification: PHYSICAL SCIENCES

Zeinab Al-Rekabi[*†] and Sonia Contera[*†]

[*]Clarendon Laboratory, Department of Physics, University of Oxford, Parks Road, OX1 3PU, Oxford, UK

Keywords: DPPC, Cholesterol, Viscoelasticity, Multifrequency AFM, AM-FM AFM

[†] Corresponding authors: zeinab.al-rekabi@physics.ox.ac.uk or s.antoranzcontera1@physics.ox.ac.uk

Abstract

The physical properties of lipid bilayers comprising the cell membrane occupy the current spotlight of membrane biology. Their traditional representation as a passive two-dimensional fluid has gradually been abandoned in favor of a more complex picture; an anisotropic time-dependent viscoelastic biphasic material, capable of transmitting or attenuating mechanical forces that regulate biological processes. In establishing new models, quantitative experiments are necessary when attempting to develop suitable techniques for dynamic measurements. Here we map both the elastic and viscous properties of the model system 1, 2-dipalmitoyl-sn-glycero-3-phosphocholine (DPPC) lipid bilayers using multifrequency atomic force microscopy (AFM), namely amplitude modulation-frequency modulation (AM-FM) AFM imaging in an aqueous environment. Furthermore, we investigate the effect of cholesterol (Chol) on the DPPC bilayer in concentrations from 0 to 60%. The AM-AFM quantitative maps demonstrate that at low Chol concentrations, the lipid bilayer displays a distinct phase separation and is elastic; whereas at higher Chol concentration, the bilayer appears homogenous and exhibits both elastic and viscous properties. At low Chol contents, the $E_{storage}$ modulus (elastic) dominates. As the Chol insertions increases, higher energy is dissipated; and although the bilayer stiffens (increase in $E_{storage}$) the viscous component dominates (E_{loss}). Our results provide evidence that the lipid bilayer exhibits both elastic and viscous properties that are modulated by the presence of Chol, which may affect the propagation (elastic) or attenuation (viscous) of mechanical signals across the cell membrane.

Significance Statement

The lipid bilayer mediates a number of cellular processes including cell recognition, signaling, transfer of ions, adhesion and fusion. In orchestrating these functions, the cell membrane behaves as both an elastic and a viscous material. Although the physical properties of the lipid bilayer have been extensively studied, a thorough description of the viscoelasticity of the membrane is significantly less well characterized. In our study, we utilize multifrequency atomic force microscopy (AFM) as a tool to extract quantitative viscoelastic information of a model lipid system with molar fraction inserts of cholesterol (Chol). Using this approach, we provide evidence that the lipid bilayer appears to exhibit both elastic and viscous properties, an important aspect in its role in mechanotransduction.

\body

Introduction

The cell membrane is a highly-specialized compartment, holding many essential cellular functions including transport of molecules, communication and metabolic properties (1). Mammalian cell membranes consist of a lipid bilayer composed of amphiphilic molecules arranged in a two-dimensional fluid crystalline assembly (2). Traditionally lipid bilayers were thought to behave as 2D Newtonian fluids allowing membrane proteins to diffuse laterally (3). More recent studies have demonstrated lipid bilayers to also possess other properties including bending, area expansion and compression moduli (4) and in some cases, shear modulus (5). This is supported by the rationale that the membrane must be stiff enough to provide stability, allowing for directed propagation of mechanical signals in both lateral and orthogonal directions. Recent research highlights the need for an accurate, high-resolution quantitative description of both the elastic and viscous aspects in building a more precise physical model of the cell membrane, describing both its transport and communication functions.

Cell membranes are dynamic structures which undergo various changes across spatiotemporal measurements, from nanoscopic to microscopic and mesoscopic scales (6, 7). Lipid bilayers respond to force in a time-varying manner as nonlinear functions of strain (8). The phospholipid bilayer shows frequency-dependent changes in tension and viscosity with viscoelastic relaxation times on the order of tens of microseconds (8). In addition, previous studies have revealed that changes to local mechanical properties of the cell membrane regulate the propagation of forces in cells (9) and modulate processes

such as membrane trafficking, endocytosis, actin assembly, cell signaling and protein function (10, 11). Mechanical forces propagating through the membrane are also central to the propagation of the action potential in neurons (12) and affect the activity of membrane proteins such as ion channels (13, 14). Moreover, previous work has also shown that mechanical properties can modulate a membranes' interface with its' surrounding liquid and are able to selectively control ionic adsorption and condensation (15).

To date, the synchronized measurements of both viscous and elastic properties of lipid membranes, with high spatial resolution has not yet been reported. Further characterization of the mechanical properties of the cell membrane would supplement our current understanding of the membrane's role in mechanotransduction. Advanced dynamic atomic force microscopy (AFM) methods are particularly well poised in achieving this goal. This is firstly due to the fact that dynamic AFM provides the highest resolution microscopy of membranes in a liquid environment. Secondly, when utilizing either frequency modulation (FM) or amplitude modulation (AM) modes, dynamic AFM has been used to successfully visualize individual lipids artificially inserted in lipid bilayers with sub-nm resolution (16, 17). Moreover, these methods generated the depiction of their hydration layers (17) and mobile ions (18) at water-lipid interfaces. In addition, AFM-based force spectroscopy nanoindentation and force-clamp measurements have been used to extract the elastic moduli of several lipid bilayers and native membranes (19-21). Recent advances in multifrequency AFM have enabled the extraction of both elastic and viscous moduli from AFM observables from higher eigenmodes of the AFM cantilever (22-27). These characteristics have also been demonstrated in living cells placed under physiological conditions (28, 29). In particular, AM-FM AFM has been proposed as a method to image and measure material properties with molecular resolution (30). The method combines bimodal excitation with FM-AFM, separating topographical information from quantitative mapping. Recent studies have shown that high-resolution imaging and elastic mapping of pentameric IgM antibodies and DNA strands could be achieved in aqueous environments (31, 32).

Due to its' small dimensions, the width of the lipid bilayer (~ 6 nm) makes it particularly challenging to extract mechanical information using dynamic AFM since the indentations required to extract meaningful information must be of at least 10% of the width of the material. Here, we exemplify the broad capability of AM-FM AFM in imaging at much smaller amplitudes (~ 0.5 - 2 nm) than other multifrequency AFM techniques (> ~ 10 nm). This is due to its' unique ability to simultaneously map both the topography and the viscoelastic properties of a model system bilayer made of 1, 2-dipalmitoyl-sn-glycero-3-phosphocholine (DPPC) lipids. The technique reproduces

previously obtained values of elastic moduli obtained by AFM semi-static nanoindentation studies of DPPC bilayers (19, 20, 33), but at magnitudes faster.

Cholesterol (Chol) is a non-phospholipid membrane component that is key for modulating the mechanical properties of mammalian cell membranes. Chol is known to enhance the permeability-barrier properties of the lipid bilayer, control membrane fluidity and provide mechanical stability. Chol localizes in both trans-bilayer and lateral domains and is one of the main components of forming rafts enriched in glycosphingolipids and proteins (34, 35). Previous studies employing several techniques including nuclear magnetic resonance (NMR), differential scanning calorimetry (DSC), neutron scattering and X-ray diffraction have detailed the liquid to gel phase transitions of the lipid:Chol mixtures at large compositional space and temperature ranges (36-39). These studies therefore comprehensively describe the phase-separated behavior of phospholipid membranes in the presence of Chol insertions. AM-FM AFM can also be used to probe the effect of Chol on the material properties of the cell membrane by consolidating these afore-mentioned qualitative scales.

In this study, we used AM-FM AFM to simultaneously map the topography and viscoelastic properties of a DPPC bilayer containing Chol (DPPC:Chol mixtures) at 0, 15, 33 and 60% concentrations. Our findings provide evidence that the lipid bilayer exhibits both elastic and viscous properties and that Chol content modulates both. Therefore, we believe the lipid bilayer is exhibiting both elastic and viscous properties, which may be used by cells to modulate the propagation (elastic) or attenuation (viscous) of mechanical signals across the cell membrane.

Results & Discussion

AFM topography of DPPC:Chol

This study examined the viscoelastic properties of the DPPC:Chol (0 – 60%) system utilizing AM-FM AFM (Fig. 1). A detailed description of the AM-FM technique is given in the SI. The first resonance of AM-FM AFM is monitored in standard tapping mode (AM mode), offering the topography of lipid bilayers through its feedback on the second eigenmode amplitude. To observe the phase separation produced by Chol in the DPPC bilayers, supported lipid bilayers (SLB) with different molar fractions of Chol were imaged and their viscoelastic properties were characterized using AM-FM AFM. DPPC forms islands of bilayers of about ~ 5 nm in height. When 15% Chol is introduced in molar fractions in the DPPC mixture, two different phases coexist (Fig. 2A, B), whereas at higher Chol concentrations, we observe a more homogenous bilayer (Fig. 2C, D). The average height of the bilayer

changes from 5.1 ± 0.90 nm for pure DPPC to 1.1 ± 0.01 nm for DPPC: Chol (60%). Since the liquid-like state of the lipid bilayers show a smaller thickness than in their gel phase (40), the observed difference in height maybe related to the fluidization effect of the Chol to the DPPC bilayer.

Previous DSC studies indicate that the DPPC bilayer exhibits a phase transition that completely disappears when the % Chol content increases (41). Our findings are consistent with previous work that has shown the existence of two phases at higher molar fractions of Chol: a Chol-rich phase and a Chol-poor DPPC phase (41). These two phases exist in equilibrium with each other until the % of Chol exceeds ~30 %, where at such high Chol concentrations an enriched fluid phase in solubilized Chol is observed (42, 43). This implies that at less than 33% Chol, the melting behavior of the DPPC:Chol system is likely governed by the melting phase transition of the Chol-rich and Chol-poor DPPC domains (37, 44). Conversely, at higher Chol concentrations (33 and 60%), no phase transition is observed, which implies that the bilayer exists in the liquid-ordered regime, consistent with previous work (41). Additionally, previous NMR studies have shown that higher Chol concentrations in PC mixtures causes a broadening and eventual removal of the clear phase transitions, suggesting an increase in exchange rate between the domains (45, 46).

To understand the role that Chol plays in maintaining the mechanical behavior of the lipid bilayer using DPPC as a model system, we used the FM component of AM-FM AFM to record the amplitude (A_3) and frequency (f_3) images. In this mode, the cantilever is driven to oscillate at the third eigenmode (~ 420 kHz). Figure S1 shows the amplitude and frequency images. In the amplitude images, DPPC and DPPC:Chol (15%) appear darker than the substrate, implying that in these areas the cantilever shifts the oscillation of the higher normal mode to a lower resonant frequency, i.e. the sample appears more dissipative than the substrate (Fig. S1A, B). At higher Chol concentrations (33 and 60%), we observe a more homogenous bilayer (Fig. S1C, D), but with few darker regions.

AFM energy dissipation of organic systems has been intensively studied in ultra-high vacuum conditions (47, 48). These previous studies demonstrated that the dissipated energy reflects the mobility of the molecules interacting with the tip (47). The images (Fig. S1) obtained in this study reveal the properties of the gel phase in pure DPPC and DPPC:Chol (15%), while at increased Chol concentrations (33 and 60%), the DPPC:Chol system is in the liquid-ordered phase exhibiting higher molecular fluidity. Generally, molecules with lower fluidity form islands and those with a higher fluidity tend to flexibly change their distribution to surround the islands. Our results are in agreement with previous work that utilized FM-AFM to study the molecular arrangement of the DPPC:Chol

system (49). Taken together, our findings demonstrate that at low Chol concentrations the lipid bilayer exhibits a distinct phase separation and is elastic; whereas at higher Chol concentration the bilayer is homogenous and displays both elastic and viscous properties.

Viscoelastic mapping of DPPC:Chol

Recently, dual-beam optical trap and lateral shear flow techniques have demonstrated the viscoelastic behavior of lipids (5, 50). Furthermore, these experiments have demonstrated apparent viscoelastic deformation of lipid bilayer vesicles (50) and membrane fluidity at lower frequencies (5). Herein, to qualitatively evaluate the elastic and viscous properties of DPPC:Chol (0-60%) we used AM-FM AFM to map the $E_{storage}$, E_{loss} and loss tangent (tanδ) of the SLBs with different molar fractions of Chol at higher frequencies (~ 150 – 420 kHz). The measured loss tangent is the ratio of the dissipated (E_{loss}) to stored ($E_{storage}$) power in the AFM tip-sample interaction. In the quantitative $E_{storage}$ maps, the DPPC and DPPC:Chol (15%) appear darker than the substrate, suggesting that the material is more dissipative than the background with values for DPPC: ~ 63 MPa and DPPC:Chol (15%): ~ 85 MPa, (Fig. 3A, B and Table S1). At higher Chol concentrations (33 and 60%), $E_{storage}$ maps appear homogenous, exhibiting higher elastic moduli, (DPPC:Chol (33%): ~225 MPa and DPPC:Chol (60%): 304 MPa), (Fig. 3C, D and Table S1). These findings demonstrate that the presence of Chol leads to the stiffening of the SLB.

The corresponding E_{loss} maps of the SLB with different Chol concentrations showed similar behaviors as the $E_{storage}$ maps. In the absence of Chol or with 15% Chol, the SLBs still appeared more dissipative than the solid mica substrate and with values of DPPC: ~ 89 MPa and DPPC:Chol (15%): ~ 99 MPa, (Fig. 3A, B and Table S1). As the molar fraction of Chol increased (33 and 60%), the SLBs appeared both homogenous and more dissipative than the SLB with 0 or 15% Chol (DPPC:Chol (33%): ~ 487 MPa and DPPC:Chol (60%): ~ 429 MPa), (Fig. 3C, D and Table S1). It is important to note that at higher Chol concentrations, the SLBs appear to show both elastic and viscous regions. Chol molecules are known to dissipate less energy in the fluid membranes and dissipate more energy in the gel-to-liquid crystalline phase transition of the lipid bilayer (51).

To characterize the viscoelastic behavior of the lipid bilayer, we determined the loss tangent tanδ from the second mode amplitude and phase (52). The loss tangent images (Fig. 3) exhibit essentially the same congruent, but inverted, pattern compared to the corresponding $E_{storage}$ and E_{loss} images. In the tanδ map, the DPPC and DPPC:Chol (15%) appeared lighter than the substrate, suggesting that the material dissipated greater energy than stored (Fig. 3A, B). Previously, the

viscoelastic loss tangent has been used to identify phase or melting transitions in polymers (53). In examining the viscoelastic behavior of DPPC:Chol mixtures with different molar fractions of Chol, we found a peak in the value of tanδ in pure DPPC compared to the other DPPC:Chol mixtures, implying a more dominant role of the elastic response (Fig. S2 and S3). As the Chol concentration increased, the tanδ maps also demonstrated the homogeneity of the SLB at these increased concentrations (33 and 60%) (Fig. 3C, D). However, lighter inclusions can be found in the SLBs, suggesting that they may be more viscous than the surrounding area (Fig. 3C, D). This finding suggests that these lighter regions are less ordered than their surroundings. Congruent with the FM-AFM data, our findings imply that SLBs with different molar fractions of Chol exhibit both elastic and viscous properties. AFM loss tangent imaging as a function of molar fractions of Chol can therefore, provide valuable information for understanding the mechanical and topographical heterogeneity of the DPPC:Chol mixtures.

Storage and loss moduli of DPPC:Chol mixtures

When the two phases coexist, the phase with 0 to low (15%) Chol concentrations maintains approximately constant $E_{storage}$ (DPPC: ~ 63 MPa and DPPC:Chol (15%): ~ 85 MPa) and E_{loss} (DPPC: ~ 89 MPa and DPPC:Chol (15%): ~ 99 MPa) moduli, while the other phase shows a steady increase in $E_{storage}$ (DPPC:Chol (33%): ~225 MPa and DPPC:Chol (60%): 304 MPa) and E_{loss} (DPPC:Chol (33%): ~ 487 MPa and DPPC:Chol (60%): ~ 429 MPa) moduli that eventually saturates with increasing Chol content (Table S1). The results are summarized in figure 4, wherein the increase in elastic and viscous components with increasing Chol fraction of the DPPC:Chol system can be observed. However, the trend does not appear to be linear. Between 0 to 15% Chol, we observe constant $E_{storage}$ and E_{loss}, where both elastic and viscous properties of the DPPC:Chol system exist.

The presence of Chol is required for normal functioning of mammalian plasma membranes (51). In fluid-phase lipids, Chol decreases membrane fluidity whereas in gel-phase lipids, Chol increases the membrane fluidity forming the so-called liquid-ordered phase (54). This phase is characterized by very close intermolecular spacing, a lack of long-range order and an increased distance between lipid headgroups (45). Here, we find that in the absence of Chol concentrations, the DPPC:Chol system shows a $E_{storage}$ value that is consistent with previous studies using semi-static AFM studies (19, 20, 33). These studies provide the Young's modulus, an intensive property that characterizes a material, independently of its geometry. However, other techniques provide the shear modulus (5, 55, 56), describing the materials response to shear stresses. For anisotropic materials such as the lipid bilayer, which exhibit differing responses to stress or strain when applied in different directions, the relationship between the Young's modulus and shear modulus is not as trivial. In

microrheological studies (55, 56), thermally driven particle trajectories are tracked as they contain information regarding the linear viscoelastic response of the material. A frequency-dependent complex shear modulus can be obtained, which typically consists of the elastic storage modulus and the viscous loss modulus. Furthermore, increasing the molar fraction of Chol (15 %) did not significantly change the $E_{storage}$ modulus. Though, DPPC:Chol (0 and 15%) also exhibits viscous behavior, the E_{loss} moduli appears comparable to the $E_{storage}$ moduli. This behavior may be explained by the fact that the small addition of Chol (15%) in the SLBs can increase the fluidity of the layer as observed elsewhere (20, 49).

However, at higher Chol concentrations (33 and 60 %), both the $E_{storage}$ and E_{loss} increased at 33% Chol, eventually saturating above that molar fraction (60% Chol). Interestingly, it appears that as the Chol concentration increases, the DPPC:Chol system appears both elastic and more viscous. This finding implies that under physiological Chol concentrations (~ 30 % Chol), the lipid bilayer is likely to behave more like a viscoelastic material, displaying both elastic and viscous properties. Previous work has shown that an excess of Chol in pulmonary surfactant films may be forced to interact with the fluid phase lipids, making areas of the SLBs more rigid (57). Consistent with this study, we find that the $E_{storage}$ moduli increased as Chol concentrations in the SLBs increased (Fig. 3C, D and Fig. 4). Moreover, the DPPC:Chol (33 and 60%) also showed an increase in the E_{loss} moduli. By increasing the Chol concentration, we believe more hydrogen bonds are likely forming allowing the system to dissipate more energy and therefore, exhibit increased viscoelasticity and relaxation time. It is well-established that Chol forms hydrogen bonds with the phosphate oxygens of the polar heads of the DPPC phospholipids (58). In another study, FM-AFM images of DPPC:Chol bilayer in the liquid-ordered phase also showed higher energy dissipation values compared to pure DPPC in the gel phase, reflecting increased molecular fluidity due to Chol insertions (49), which may increase the viscous properties of the DPPC:Chol system.

Based on previous studies on the viscoelasticity of lipid bilayers, it can be expected that the storage and loss moduli depend on the frequency at which they are being probed. In previous studies, the values for $E_{storage}$ and E_{loss} moduli have been validated at low frequencies (~ 1 kHz) (5, 59-61), although not at high frequencies (~ 150 – 420 kHz) as presented in this work. In contrast to our findings, low values for the elastic and viscous moduli have been reported in the afore-mentioned studies. Several reasons can account for these observed differences: (I) the studies used microrheological techniques; (II) the models used in those experiments have not been validated for high frequencies; and finally (III) it can be expected that viscoelastic materials exhibit higher moduli

when probed at higher frequencies due to their time-dependent responses. AM-FM AFM uses the Kelvin-Voight model to calculate the viscoelasticity of the material. In this description, the time scale of the response of the material can be calculated (within the assumptions made in the AM-FM technique, as discussed in detail in the SI), using the formula $\tau = \frac{\tan\varphi}{2\pi f}$. The measured relaxation timescales range from ~ 1.66 μsec to ~ 2.64 μsec for DPPC bilayers containing 0 to 60% Chol. Our results suggest that higher molar fractions of Chol produce more energy dissipated from the SLBs and therefore, an increase in the time it takes the system to relax after it has been deformed. The advantage of probing the higher frequencies (~1 Hz – 100 kHz) has recently been demonstrated in assessing cytoskeletal dynamics of living cells (62). This study found that the mechanical response at high frequency provided valuable insight into the morphological and dynamical state of the cytoskeleton. Therefore, high frequency mechanics may be used to characterize the mechanical phenotype of living cells in physiological and pathological environments.

It is believed that excess Chol may cause (I) the lateral spacing of lipid head groups to increase; and (II) the DPPC heads to dissociate through the formation of hydrogen bonding with the ester linkages of the glycerol backbone of the lipids (63). This loosening of the inter-molecular association between the lipids reduces the van der Waals interactions between the hydrocarbon chains (63), increasing the liquid-ordered phase of the bilayer. This mechanism could be responsible for the increase in the viscous properties of the DPPC bilayer with the incorporation of Chol. Furthermore, it is likely that increased lipid ordering in the membrane may enhance the ability of permeant molecules to diffuse through the lipid bilayer. Therefore, it is possible that in the gel phase DPPC, the SLB's order allows permeation of molecules through the bilayer. This behavior is likely to be related to the observed elastic behavior of the lipid bilayer (Fig. 3A, B and Fig. 4). Recent work in organic semiconductor materials has shown that the less ordered and more amorphous the poly(3-hexylthiophene) films were, the less permeable the material was to ions, and the less likely it conducted electrons (64). This is an interesting finding because it demonstrates that signal propagation is poor when the material is dissipative compared to when poly(3-hexylthiophene) is rigid and crystalline (64). This finding can be compared to cell membranes, where it has been postulated that an elastic bilayer can propagate signal transductions through the membrane much easier than a more dissipative bilayer (10). Furthermore, changes in the mechanical properties of the membranes' interface with the aqueous environment can affect ionic adsorption across the bilayer (15). Therefore, local changes to the viscoelastic properties of the cell membrane are likely regulating the propagation of forces and modulating various physiological and pathological processes.

Conclusion

The mechanisms by which the mechanical properties of the membrane influence signal transduction still remain poorly understood. By modulating both changes in amplitude and frequency utilizing AM-FM AFM, we have investigated the viscoelasticity of model biological membranes consisting of DPPC molecules and different molar fractions of Chol. Our values of elasticity for DPPC agree with previous reports using semi-static AFM indentations, therefore validating the accuracy of our findings. Furthermore, our data implies that DPPC:Chol (60%) shows higher energy dissipation when compared to the gel phase DPPC. Additionally, our results provide evidence that the lipid bilayer is exhibiting both elastic and viscous properties, which is likely to affect the propagation (elastic) or attenuation (viscous) of mechanical signals across the cell membrane. Further investigation is needed to provide deeper insights into the mechanisms that regulate and modulate the physical properties of the lipid bilayer and its role in mechanotransduction in physiological and pathological processes.

Materials and Methods

Detailed information on the materials and methods is included in the **SI Materials and Methods**.

1, 2-dipalmitoyl-sn-glycero-3-phosphocholine (DPPC; Sigma-Aldrich, Scotland, UK) and Chol (Avanti, Alabaster, AL, USA) were both separately dissolved in chloroform (Sigma-Aldrich, Irvine, Scotland, UK) at stock concentrations of 0.82 mM and 1.29 mM respectively, (Fig. 1A).

Competing Interests

The authors declare no competing interests.

Author contributions

ZAR and SC conceived and designed the experiments. ZAR performed the experiments. ZAR and SC analyzed the data. ZAR and SC wrote the paper. All authors gave final approval and agree to be accountable for all aspects of the work.

Acknowledgments

This work was supported by the EPSRC funded project NeuroPulse (EP/N020987/1). We acknowledge the helpful discussions with Jacob Seifert (University of Oxford), Calum Gabbutt (University of Oxford), Nazia S. Siddiqui (Bristol University) and Prof. Antoine Jerusalem (University of Oxford).

References

1. Lombard J (2014) Once upon a time the cell membranes: 175 years of cell boundary research. *Biol Direct* 9(32):1-35.
2. Singer SJ & Nicolson GL (1972) The fluid mosaic model of the structure of cell membranes. *Science* 175(4023):720-731.
3. van Meer G, Voelker DR, & Feigenson GW (2008) Membrane lipids: where they are and how they behave. *Nat Rev Mol Cell Bio* 9(2):112-124.
4. Tyler WJ (2012) The mechanobiology of brain function. *Nat Rev Neuroscience* 13(12):867-878.
5. Espinosa G, Lopez-Montero I, Monroy F, & Langevin D (2011) Shear rheology of lipid monolayers and insights on membrane fluidity. *Proc Natl Acad Sci USA* 108(15):6008-6013.
6. Pastor RW & Feller SE (1996) Time scales of lipid dynamics and molecular dynamics. Biological Membranes, eds Merz Jr. KM, Raux B (Birkhauser, Boston), pp 3-29.
7. Heimburg T (2008) Thermal Biophysics of Membranes. (Wiley, Weinheim), p 378.
8. Crawford GE & Earnshaw JC (1987) Viscoelastic relaxation of bilayer lipid membranes. Frequency-dependent tension and membrane viscosity. *Biophys J* 52(1):87-94.
9. Janmey PA & Kinnunen PKJ (2006) Biophysical properties of lipids and dynamic membranes. *Trends Cell Biol* 16(10):538-546.
10. Anishkin A, Loukin SH, Teng JF, & Kung C (2014) Feeling the hidden mechanical forces in lipid bilayer is an original sense. *Proc Natl Acad Sci USA* 111(22):7898-7905.
11. Diz-Munoz A, Fletcher DA, & Weiner OD (2013) Use the force: membrane tension as an organizer of cell shape and motility. *Trends Cell Biol* 23(2):47-53.
12. Heimburg T & Jackson AD (2005) On soliton propagation in biomembranes and nerves. *Proc Natl Acad Sci USA* 102(28):9790-9795.
13. Dong YY, *et al.* (2015) K2P channel gating mechanisms revealed by structures of TREK-2 and a complex with Prozac. *Science* 347(6227):1256-1259.
14. Morris CE (1990) Mechanosensitive Ion Channels. *J Membrane Biol* 113(2):93-107.

15. Contera SA, Voitchovsky K, & Ryan JF (2010) Controlled ionic condensation at the surface of a native extremophile membrane. *Nanoscale* 2(2):222-229.
16. Voitchovsky K, Kuna JJ, Contera SA, Tosatti E, & Stellacci F (2010) Direct mapping of the solid-liquid adhesion energy with subnanometre resolution. *Nat Nanotech* 5(6):401-405.
17. Fukuma T, Higgins MJ, & Jarvis SP (2007) Direct imaging of individual intrinsic hydration layers on lipid bilayers at Angstrom resolution. *Biophys J* 92(10):3603-3609.
18. Fukuma T, Higgins MJ, & Jarvis SP (2007) Direct imaging of lipid-ion network formation under physiological conditions by frequency modulation atomic force microscopy. *Phys Rev Lett* 98(10):106101.
19. Picas L, Rico F, & Scheuring S (2012) Direct Measurement of the Mechanical Properties of Lipid Phases in Supported Bilayers. *Biophys J* 102(1):L1-L3.
20. Zhou JH, Liang DH, & Contera S (2015) Effect of intra-membrane C-60 fullerenes on the modulus of elasticity and the mechanical resistance of gel and fluid lipid bilayers. *Nanoscale* 7(40):17102-17108.
21. Voitchovsky K, Contera SA, Kamihira M, Watts A, & Ryan JF (2006) Differential stiffness and lipid mobility in the leaflets of purple membranes. *Biophys J* 90(6):2075-2085.
22. Solares SD & Chawla G (2010) Frequency response of higher cantilever eigenmodes in bimodal and trimodal tapping mode atomic force microscopy. *Meas Sci Technol* 21(12):125502.
23. Xu X, Melcher J, Basak S, Reifenberger R, & Raman A (2009) Compositional Contrast of Biological Materials in Liquids Using the Momentary Excitation of Higher Eigenmodes in Dynamic Atomic Force Microscopy. *Phys Rev Lett* 102(6):060801.
24. Dietz C, *et al.* (2008) Nanotomography with enhanced resolution using bimodal atomic force microscopy. *Appl Phys Lett* 92(14):143107.
25. Preiner J, Tang JL, Pastushenko V, & Hinterdorfer P (2007) Higher harmonic atomic force microscopy: Imaging of biological membranes in liquid. *Phys Rev Lett* 99(4):046102.
26. Proksch R (2006) Multifrequency, repulsive-mode amplitude-modulated atomic force microscopy. *Appl Phys Lett* 89(11):113121.
27. Rodriguez TR & Garcia R (2004) Compositional mapping of surfaces in atomic force microscopy by excitation of the second normal mode of the microcantilever. *Appl Phys Lett* 84(3):449-451.
28. Raman A, *et al.* (2011) Mapping nanomechanical properties of live cells using multi-harmonic atomic force microscopy. *Nat Nanotech* 6(12):809-814.

29. Cartagena A & Raman A (2014) Local Viscoelastic Properties of Live Cells Investigated Using Dynamic and Quasi-Static Atomic Force Microscopy Methods. *Biophys J* 106(5):1033-1043.
30. Garcia R & Proksch R (2013) Nanomechanical mapping of soft matter by bimodal force microscopy. *Eur Polym J* 49(8):1897-1906.
31. Martinez-Martin D, Herruzo ET, Dietz C, Gomez-Herrero J, & Garcia R (2011) Noninvasive Protein Structural Flexibility Mapping by Bimodal Dynamic Force Microscopy. *Phys Rev Lett* 106(19):198101.
32. Kocun M, Labuda A, Meinhold W, Revenko I, & Proksch R (2017) Fast, High Resolution, and Wide Modulus Range Nanomechanical Maping with Bimodal Tapping Mode. *ACS Nano* DOI. 10.1021/acsnano.7b04530.
33. Delorme N & Fery A (2006) Direct method to study membrane rigidity of small vesicles based on atomic force microscope force spectroscopy. *Phys Rev E* 74(3):030901.
34. Jacobson K & Dietrich C (1999) Looking at lipid rafts? *Trends Cell Biol* 9(3):87-91.
35. Brown DA & London E (2000) Structure and function of sphingolipid- and cholesterol-rich membrane rafts. *J Biol Chem* 275(23):17221-17224.
36. Marsh D (2010) Liquid-ordered phases induced by cholesterol: A compendium of binary phase diagrams. *BBA-Biomembranes* 1798(3):688-699.
37. Mcmullen TPW & Mcelhaney RN (1995) New Aspects of the Interaction of Cholesterol with Dipalmitoylphosphatidylcholine Bilayers as Revealed by High-Sensitivity Differential Scanning Calorimetry. *BBA-Biomembranes* 1234(1):90-98.
38. Mortensen K, Pfeiffer W, Sackmann E, & Knoll W (1988) Structural-Properties of a Phosphatidylcholine-Cholesterol System as Studied by Small-Angle Neutron-Scattering - Ripple Structure and Phase-Diagram. *Biochim Biophys Acta* 945(2):221-245.
39. Karmakar S, Raghunathan VA, & Mayor S (2005) Phase behaviour of dipalmitoyl phosphatidylcholine (DPPC)-cholesterol membranes. *J Phys-Condens Mat* 17(14):S1177-S1182.
40. Seeger HM, Marino G, Alessandrini A, & Facci P (2009) Effect of Physical Parameters on the Main Phase Transition of Supported Lipid Bilayers. *Biophys J* 97(4):1067-1076.
41. Redondo-Morata L, Giannotti MI, & Sanz F (2012) Influence of Cholesterol on the Phase Transition of Lipid Bilayers: A Temperature-Controlled Force Spectroscopy Study. *Langmuir* 28(35):12851-12860.
42. Sankaram MB & Thompson TE (1990) Interaction of Cholesterol with Various Glycerophospholipids and Sphingomyelin. *Biochemistry* 29(47):10670-10675.

43. Sankaram MB & Thompson TE (1991) Cholesterol-Induced Fluid-Phase Immiscibility in Membranes. *Proc Natl Acad Sci USA* 88(19):8686-8690.

44. McMullen TPW & McElhaney RN (1996) Physical studies of cholesterol-phospholipid interactions. *Curr Opin Colloid In* 1(1):83-90.

45. Clarke JA, Heron AJ, Seddon JM, & Law RV (2006) The diversity of the liquid ordered (L-o) phase of phosphatidylcholine/cholesterol membranes: A variable temperature multinuclear solid-state NMR and X-ray diffraction study. *Biophys J* 90(7):2383-2393.

46. Huang TH, Lee CWB, Dasgupta SK, Blume A, & Griffin RG (1993) A C-13 and H-2 Nuclear-Magnetic-Resonance Study of Phosphatidylcholine Cholesterol Interactions - Characterization of Liquid-Gel Phases. *Biochemistry* 32(48):13277-13287.

47. Fukuma T, Kobayashi K, Yamada H, & Matsushige K (2004) Noncontact atomic force microscopy study of copper-phthalocyanines: Submolecular-scale contrasts in topography and energy dissipation. *J Appl Phys* 95(9):4742-4746.

48. Fukuma T, Ichii T, Kobayashi K, Yamada H, & Matsushige K (2004) Molecular-scale noncontact atomic force microscopy contrasts in topography and energy dissipation on c(4x2) superlattice structures of alkanethiol self-assembled monolayers. *J Appl Phys* 95(3):1222-1226.

49. Asakawa H & Fukuma T (2009) The molecular-scale arrangement and mechanical strength of phospholipid/cholesterol mixed bilayers investigated by frequency modulation atomic force microscopy in liquid. *Nanotechnology* 20(26):264008.

50. Wu SH, *et al.* (2015) Viscoelastic deformation of lipid bilayer vesicles. *Soft Matter* 11(37):7385-7391.

51. Alberts B (2002) Molecular Biology of the Cells. (Garland Science, New York), 4th Ed. pp 617-650.

52. Proksch R & Yablon DG (2012) Loss tangent imaging: Theory and simulations of repulsive-mode tapping atomic force microscopy. *Appl Phys Lett* 100(7):073106.

53. Proksch R, *et al.* (2016) Practical loss tangent imaging with amplitude-modulated atomic force microscopy. *J Appl Phys* 119(13):134901.

54. Bloom M, Evans E, & Mouritsen OG (1991) Physical-Properties of the Fluid Lipid-Bilayer Component of Cell-Membranes - a Perspective. *Q Rev Biophys* 24(3):293-397.

55. Crocker JC & Hoffman BD (2007) Multiple-particle tracking and two-point microrheology in cells. *Methods Cell Biol* 83:141-178.

56. Waigh TA (2005) Microrheology of complex fluids. *Rep Prog Phys* 68:685-742.

57. Leonenko Z, Finot E, Vassiliev V, & Amrein M (2006) Effect of cholesterol on the physical properties of pulmonary surfactant films: Atomic force measurements study. *Ultramicroscopy* 106(8-9):687-694.
58. Bonn M, *et al.* (2004) A molecular view of cholesterol-induced condensation in a lipid monolayer. *J Phys Chem B* 108(50):19083-19085.
59. Cicuta P, Keller SL, & Veatch SL (2007) Diffusion of liquid domains in lipid bilayer membranes. *J Phys Chem B* 111(13):3328-3331.
60. Kim K, Choi SQ, Zell ZA, Squires TM, & Zasadzinski JA (2013) Effect of cholesterol nanodomains on monolayer morphology and dynamics. *Proc Natl Acad Sci USA* 110(33):E3054-E3060.
61. Kim K, Choi SQ, Zasadzinski JA, & Squires TM (2011) Interfacial microrheology of DPPC monolayers at the air-water interface. *Soft Matter* 7(17):7782-7789.
62. Rigato A, Miyagi A, Scheuring S, Miyagi A, & Rico F (2017) High-Frequency Microrheology reveals Cytoskeleton Dynamics in Living Cells. *Nat Phys* 13(8):771-775.
63. Bhattacharya S & Haldar S (2000) Interactions between cholesterol and lipids in bilayer membranes. Role of lipid headgroup and hydrocarbon chain-backbone linkage. *BBA-Biomembranes* 1467(1):39-53.
64. Giridharagopal R, *et al.* (2017) Electrochemical strain microscopy probes morphology-induced variations in ion uptake and performance in organic electrochemical transistors. *Nat Maters* 16(7):737-742.

Figure Legend

Fig. 1 Schematic of the supported lipid bilayer (SLB) preparation. (A) Chemical structures of DPPC and Chol. (B) Diagram describing the SLB preparation process by vesicle fusion. (C) The schematic of operation for AM-FM AFM and a 3-dimensional topographical representation of the SLB. In brief, two separate excitation signals are combined to excite the cantilever resonances simultaneously. The resulting cantilever deflection is analyzed to determine the response at each resonance. The first resonance operates in normal tapping mode (AM mode). The amplitude A_2 controls the vertical feedback loop for the standard tapping mode topography, while A_2 and the phase φ_2 give the values for the loss tangent. The second resonance operates in the FM mode. Changes in resonance frequency determine the elasticity, while changes in the amplitude A_3 give the dissipation information.

Fig. 2 Topographical images and profiles of DPPC:Chol mixtures. The first resonance (AM-mode) provides the topography of our model system at different Chol concentrations: (A) pure DPPC (scan size: 2.0 μm); (B) DPPC:Chol (15%) (scan size: 2.2 μm); (C) DPPC:Chol (33%) (scan size: 5.5 μm); and (D) DPPC:Chol (60%) (scan size: 2.9 μm). The height profiles corresponding to the lines drawn over the images displayed. Scale bar: 500 nm (left-hand corner).

Fig. 3 Quantitative viscoelastic mapping of DPPC:Chol mixtures. The E_{storage} and E_{loss} maps for (A) the pure DPPC (scan size: 2.7 μm) and (B) DPPC:Chol (15%) (scan size: 4.6 μm) appeared darker than the substrate, suggesting that the material is more dissipative than the background. Their corresponding loss tangent images (tanδ) shows essentially the same congruent, but inverted, pattern compared to the corresponding E_{storage} and E_{loss} images. In the tanδ map, the DPPC and DPPC:Chol (15%) appears lighter than the substrate, suggesting that the material dissipates greater energy than which it stores. At

higher Chol concentrations: (C) 33 mol % (scan size: 5.4 μm) and (D) 60 mol % (scan size: 4.9 μm), the $E_{storage}$ and E_{loss} maps of the system appear homogenous; however, the membrane appears to stiffen, becoming more viscous. In addition, the corresponding tanδ maps also demonstrate the homogeneity of the model system at these increased concentrations (33 and 60%) with lighter inclusions in the monolayer, suggesting that they may be more viscous than the surrounding SLBs. Scale bar: 500 nm (left-hand corner).

Fig. 4 Storage and loss moduli of DPPC:Chol mixtures. The mean $E_{storage}$ (red) and E_{loss} (black) of the DPPC:Chol as function of the percentage molar fraction of Chol. The error bars correspond to the SD.

Supporting Information

SI Materials and Methods

Supported lipid bilayers (SLB). SLBs were obtained through the commonly used method, small unilamellar vesicle fusion (1). Circular mica surfaces (Ted Pella, Redding, CA, USA) were used as SLB substrates for the experiments. Initially, mica surfaces were mounted onto metal discs using high-vacuum silicone grease (Dow Corning, Midland, MI, USA). Freshly cleaved mica supports were initially lubricated with 100 ml of 20 mM NaCl. This was followed by placing 7 µl of SUV suspension onto the mica and allowing them to settle at room temperature for 20 min. Next, the samples were rinsed several times with 20 mM NaCl to avoid unfused vesicles, but were always kept hydrated. The samples were then heated to 60◦C for 45 mins. The SLB preparation process is shown in Fig. 1B.

AM-FM AFM. After slowly cooling down the sample, it was mounted onto the Asylum Research Cypher AFM (Oxford Instruments Asylum Research, Santa Barbara, USA) and imaged. Using AM-FM mode, two separate excitation signals were combined to excite two cantilever resonances simultaneously. The principle of AM-FM operation in aqueous environment has been previously described (2-5). Briefly, the first resonance was monitored in standard tapping mode (AM mode), providing the topography through feedback on the first-resonance amplitude, (Fig. 1C). Meanwhile, the cantilever was driven to oscillate at a second resonance, where the frequency was tracked by the controller (FM mode), (Fig. 1C). This implied that a stiffer sample will shift the oscillation of the higher normal mode to a higher frequency (6-8). Since, AM-FM AFM involves the excitation of two cantilever eigenmodes (3, 4), we can therefore measure the deflection of cantilever as $z(t) = z_0 + A_2\cos(\omega_2 t - \varphi_2) + A_3\cos(\omega_3 t - \varphi_3) + O(\alpha)$, where z_0 is the mean deflection and $O(\alpha)$ contains higher order terms, which are usually very small. The amplitude of the second eigenmode (A_2) is used to track the topography of the material, while the amplitude and phase of the third eigenmode are used to map both the conservative and dissipative components of the tip-sample interaction (3, 4, 9). In brief, the bimodal excitation and detection with FM mode of the AFM under aqueous conditions, provides simultaneous information on both topography and local elastic modulus (storage), (3, 4). Furthermore, the signal of the lower frequency is used to establish the feedback mechanism as in regular FM AFM while the higher frequency is sampled to provide the elastic modulus. Therefore, in AM-FM AFM quantitative information of materials are extracted from the projection of the continuous beam deflection over the cantilever eigenmodes. Applying both energy conservation and the virial theorem to the third eigenmode (free) gives two independent equations:

$E_3^{dissipated} = -\int_0^T F_{tip-sample}(d) \cdot \dot{z}_3(t)dt = \frac{\pi k_3 A_3}{Q_3} (A_{0,3} sin\varphi_3 - A_3)$ and $V_3^{tip-sample} = \frac{1}{T}\int_0^T F_{tip-sample}(d) \cdot z_3(t)dt = -\frac{k_3 A_{0,3}}{2Q_3} A_3 cos\varphi_3$, where $E^{dissipated}$ is the energy dissipated by the tip-sample forces, $V_{tip-sample}$ is the virial tip-sample forces and $F_{tip-sample}$ is the tip-sample forces. The virial equation can be simplified using previous approximations (10) to express a relationship between the gradient of the interaction forces and phase shift of the third mode to give, $F'_{tip-sample}(d) \approx C \frac{k_3 A_{0,3}}{A_3(z_c) Q_3} cos\varphi_3(z_c)$, where $A_{0,3}$, k_3 and Q_3 are the free amplitude, spring constant and quality factor of the third eigenmode respectively. There is a correction factor, C that converges for high ratios ($A_{0,2}/A_{0,3}$) and finally, the relevant distances in the theory used for the tip-sample separation is $d = z + z_c = z_c - A_2 - A_3$. Using the Hertz contact model for a paraboloid indenter of radius R , the elasticity of the sample is related to the tip-sample stiffness by the relation $k_{int}(\delta) = 2E\sqrt{R\delta}$, where E is the elastic modulus (storage modulus) and δ is the indentation depth. Therefore, a relationship between φ_3 and E can be obtained where $F'_{tip-sample}(z_c) = 2E\sqrt{R\delta} = 2Er_c$, where r_c is the true contact radius, which has been derived in detail elsewhere (5). In the FM mode, the elastic modulus maps ($E_{storage}$) are determined by recording $A_3(x, y)$ and $\varphi_3(x, y)$ and hence we can determine those maps from the above equations, where $E = \frac{1}{2r_c} \frac{k_3 A_{0,3}}{A_3(z_c) Q_3} cos\varphi_3(z_c)$. Consequently, as described elsewhere in detail (8, 11), a loss tangent map is obtained from the amplitude and phase signals in the AM mode. Since this technique is based on the Kelvin-Voigt viscoelastic model, we know that the loss tangent is equivalent to the ratio of the dissipated energy to stored energy ($\tan\delta = E_{loss}/E_{storage}$), allowing us to obtain the loss modulus ($E_{loss} = E_{storage} \tan\delta$). In this study, AM-FM AFM was used to estimate the $E_{storage}$ and E_{loss} of DPPC:Chol (0-60%) lipid bilayers. We used OMCL-RC800PSA silicon nitride tips with a spring constant of 0.76 N/m (Olympus, Tokyo, Japan). Cantilevers were calibrated using the Sader method (12). The tip was brought in contact with the sample and the drive frequency was carefully adjusted to the resonant frequency of the second normal mode of vibration of the cantilever (f_2 ~ 150 kHz) with a larger free amplitude at (~ 50 – 100 nm). Meanwhile, the cantilever was driven at a second resonance, characterized by higher frequency (f_3 ~ 420 kHz), corresponding to the third normal mode with much smaller amplitude (~ 0.5 – 2 nm). The third mode was adjusted to keep the phase at 90° on resonance. After the method was calibrated using a sample of known elastic modulus (DPPC), the tip was retracted, and the calibration sample was replaced by the sample of interest. When the tip-to-surface approach was completed, both resonances were tuned again. The drive set-point of the second normal mode was 700-800 mV and that of the higher mode was 20 mV. A low

A_3/A_0 ensured optimal tracking of the surface topography, which was important to obtain proper results in AM-FM AFM. All results in this work are freely available from our lab by contacting the corresponding authors.

Data deposition: All results in this work have been deposited in figshare (https://figshare.com/articles/PNAS_paper_zip/5894584).

Data analysis. The images were rendered and post-processed with the software IGOR PRO 6.2 (WaveMetrics, Lake Oswego, OR, USA). Post-processing included cropping and flattening the images using the 1st, 3rd or histogram flatten order. In this study, $E_{storage}$ and E_{loss} of mixtures of DPPC, DPPC:Chol (15%), DPPC:Chol (33%) and DPPC:Chol (60%) were obtained using IGOR. Histograms were plotted for the distribution of the moduli recorded for all pixels of the image. The histograms were fitted with gaussian fits in Matlab (The MathWorks, Natick, MA, USA), providing both the mean and standard deviation (SD), (Table S1). All results presented in this work are freely available from our lab by contacting the corresponding authors. Data deposition: All results in this work have been deposited in figshare (https://figshare.com/articles/PNAS_paper_zip/5894584).

References

1. Mingeot-Leclercq MP, Deleu M, Brasseur R, & Dufrene YF (2008) Atomic force microscopy of supported lipid bilayers. *Nat Protoc* 3(10):1654-1659.
2. Kocun M, Labuda A, Meinhold W, Revenko I, & Proksch R (2017) Fast, High Resolution, and Wide Modulus Range Nanomechanical Maping with Bimodal Tapping Mode. *ACS Nano DOI: 10.1021/acsnano.7b04530.*
3. Garcia R & Proksch R (2013) Nanomechanical mapping of soft matter by bimodal force microscopy. *Eur Polym J* 49(8):1897-1906.
4. Martinez-Martin D, Herruzo ET, Dietz C, Gomez-Herrero J, & Garcia R (2011) Noninvasive Protein Structural Flexibility Mapping by Bimodal Dynamic Force Microscopy. *Phys Rev Lett* 106(19):198101.
5. Labuda A, Kocun M, Meinhold W, Walters D, & Proksch R (2016) Generalized Hertz model for bimodal nanomechanical mapping. *Beilstein J Nanotechnol* 7:970-982.
6. Guo S, *et al.* (2012) Multifrequency imaging in the intermittent contact mode of atomic force microscopy: beyond phase imaging. *Small* 8(8):1264-1269.

7. Solares SD & Chawla G (2010) Triple-frequency intermittent contact atomic force microscopy characterization: Simultaneous topographical, phase, and frequency shift contrast in ambient air. *J Appl Phys* 108(5):054901.
8. Proksch R & Yablon DG (2012) Loss tangent imaging: Theory and simulations of repulsive-mode tapping atomic force microscopy. *Appl Phys Lett* 100(7):073106.
9. Lozano JR & Garcia R (2008) Theory of multifrequency atomic force microscopy. *Physical review letters* 100(7):076102.
10. Kawai S, *et al.* (2009) Systematic achievement of improved atomic-scale contrast via bimodal dynamic force microscopy. *Phys Rev Lett* 103(22):220801.
11. Proksch R, *et al.* (2016) Practical loss tangent imaging with amplitude-modulated atomic force microscopy. *J Appl Phys* 119(13):134901.
12. Sader JE, Chon JWM, & Mulvaney P (1999) Calibration of rectangular atomic force microscope cantilevers. *Rev Sci Instrum* 70(10):3967-3969.

Supplemental Information Legends

Fig. S1 The frequency modulation (FM) component of AM-FM AFM. The second resonance provides the amplitude (A_3) and frequency (f_3) information of DPPC:Chol with various molar fractions of Chol: (A) DPPC (0 mol %; scan size: 3.5 µm); (B) 15 mol % (scan size: 5.2 µm), which appears darker than the substrate, suggesting that the material is softer than the background; (C) Both 33 mol % (scan size: 5.4 µm); and (D) 60 mol % (scan size: 3.8 µm) appear homogenous. Scale bar: 500 nm (bottom left-hand corner).

Fig. S2 Loss tangent values as function of molar fractions of Chol. The tanδ values for each respective mol % of Chol in the DPPC:Chol model system.

Fig. S3 Storage and loss moduli as a function of loss tangent values. The mean E_{storage} (red) and E_{loss} (black) of the DPPC:Chol as function of the loss tangent values (tanδ). The error bars correspond to the SD.

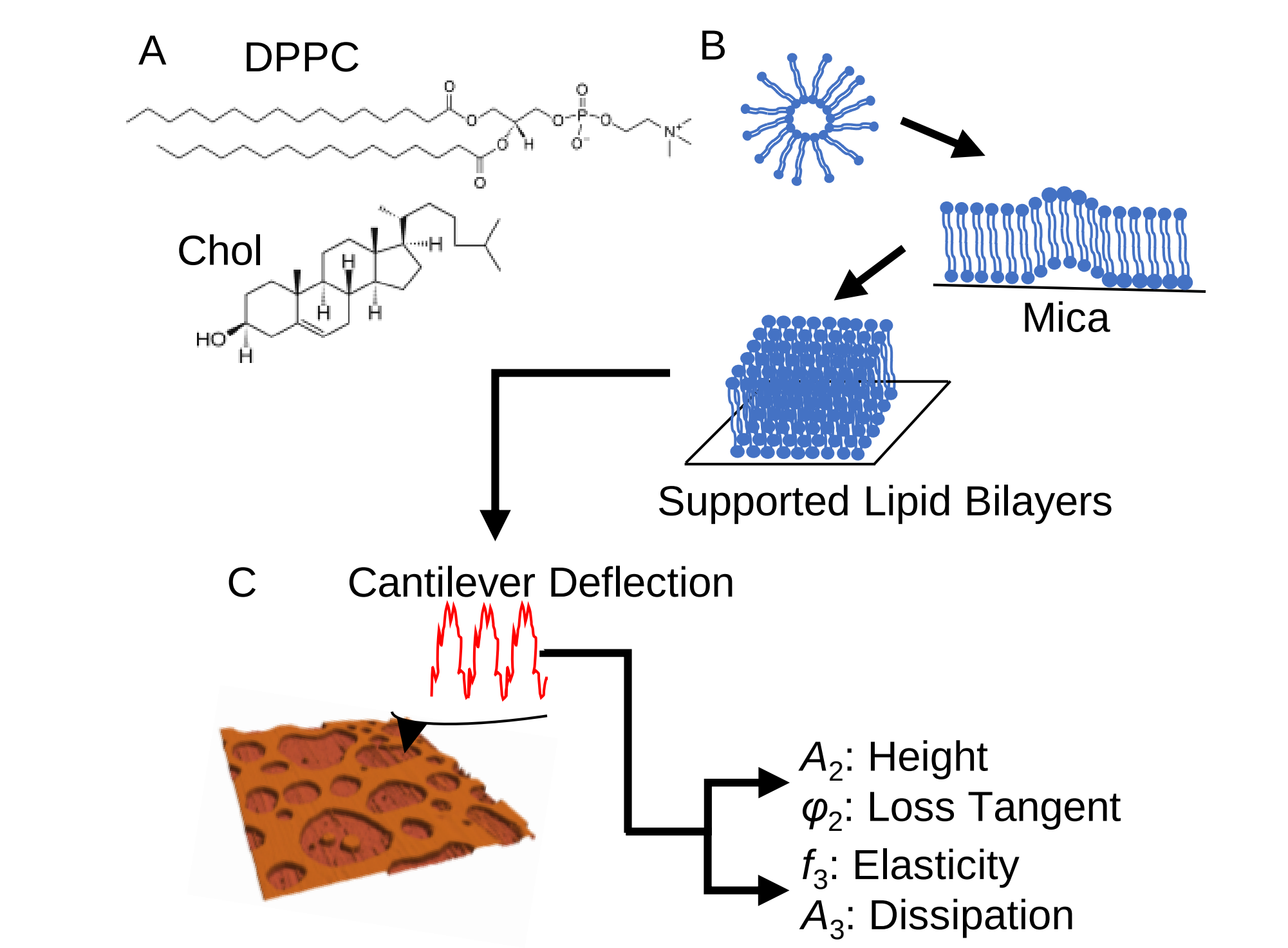
A
DPPC
Chol
B
Mica
Supported Lipid Bilayers
C
Cantilever Deflection
A_2: Height
φ_2: Loss Tangent
f_3: Elasticity
A_3: Dissipation

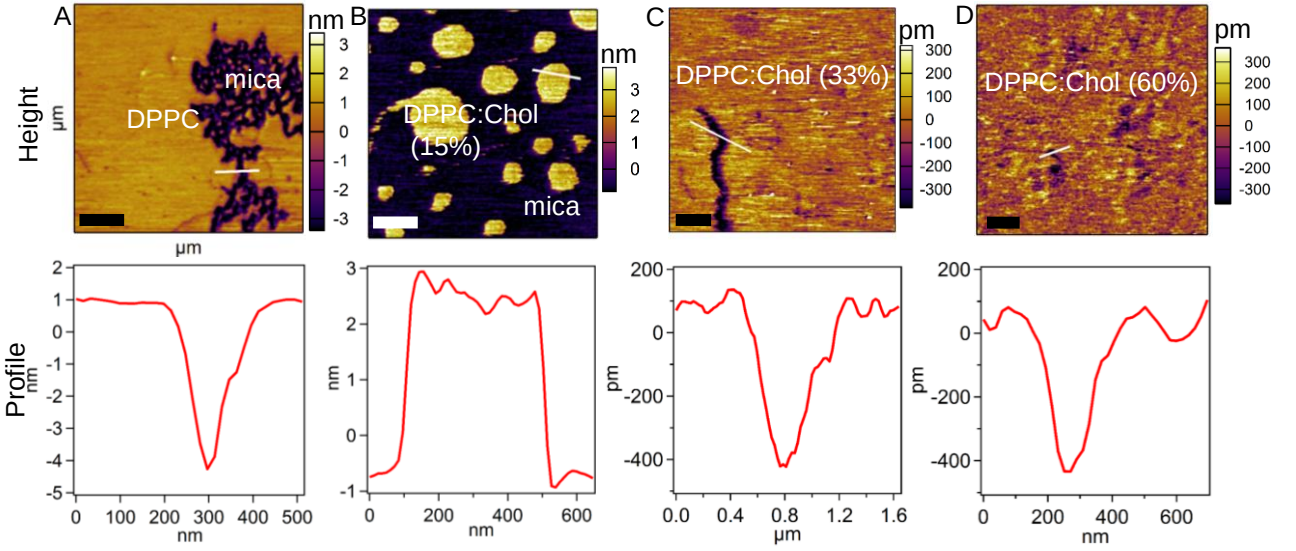
A
B
C
D
Height
Profile
mica
DPPC
DPPC:Chol
(15%)
DPPC:Chol (33%)
DPPC:Chol (60%)
nm
pm
μm

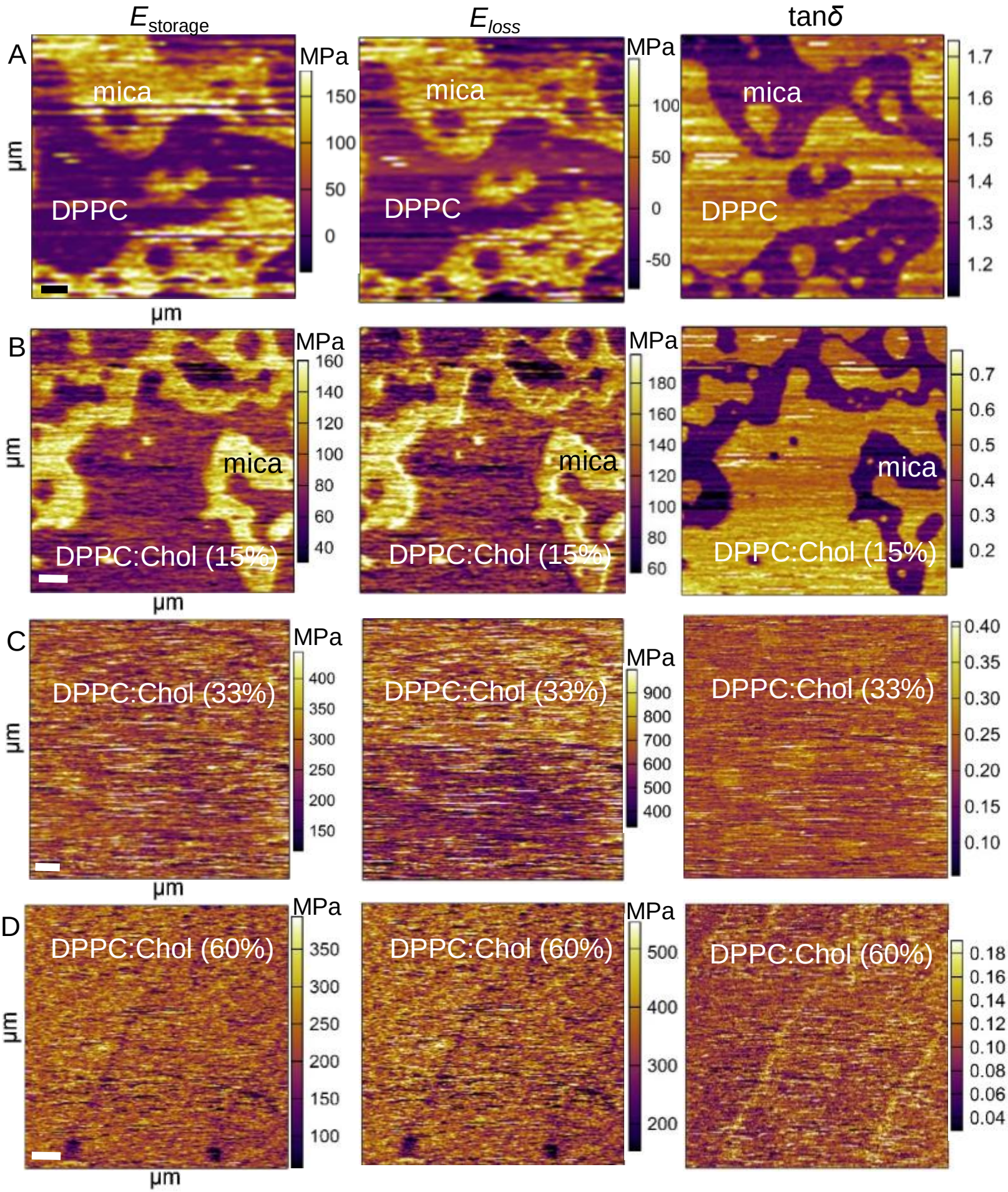
$E_{storage}$
E_{loss}
tanδ
A
mica
DPPC
MPa
150
100
50
0
100
50
0
-50
1.7
1.6
1.5
1.4
1.3
1.2
B
DPPC:Chol (15%)
160
140
120
100
80
60
40
180
160
140
120
100
80
60
0.7
0.6
0.5
0.4
0.3
0.2
C
DPPC:Chol (33%)
400
350
300
250
200
150
900
800
700
600
500
400
0.40
0.35
0.30
0.25
0.20
0.15
0.10
D
DPPC:Chol (60%)
350
300
250
200
150
100
500
400
300
200
0.18
0.16
0.14
0.12
0.10
0.08
0.06
0.04
μm

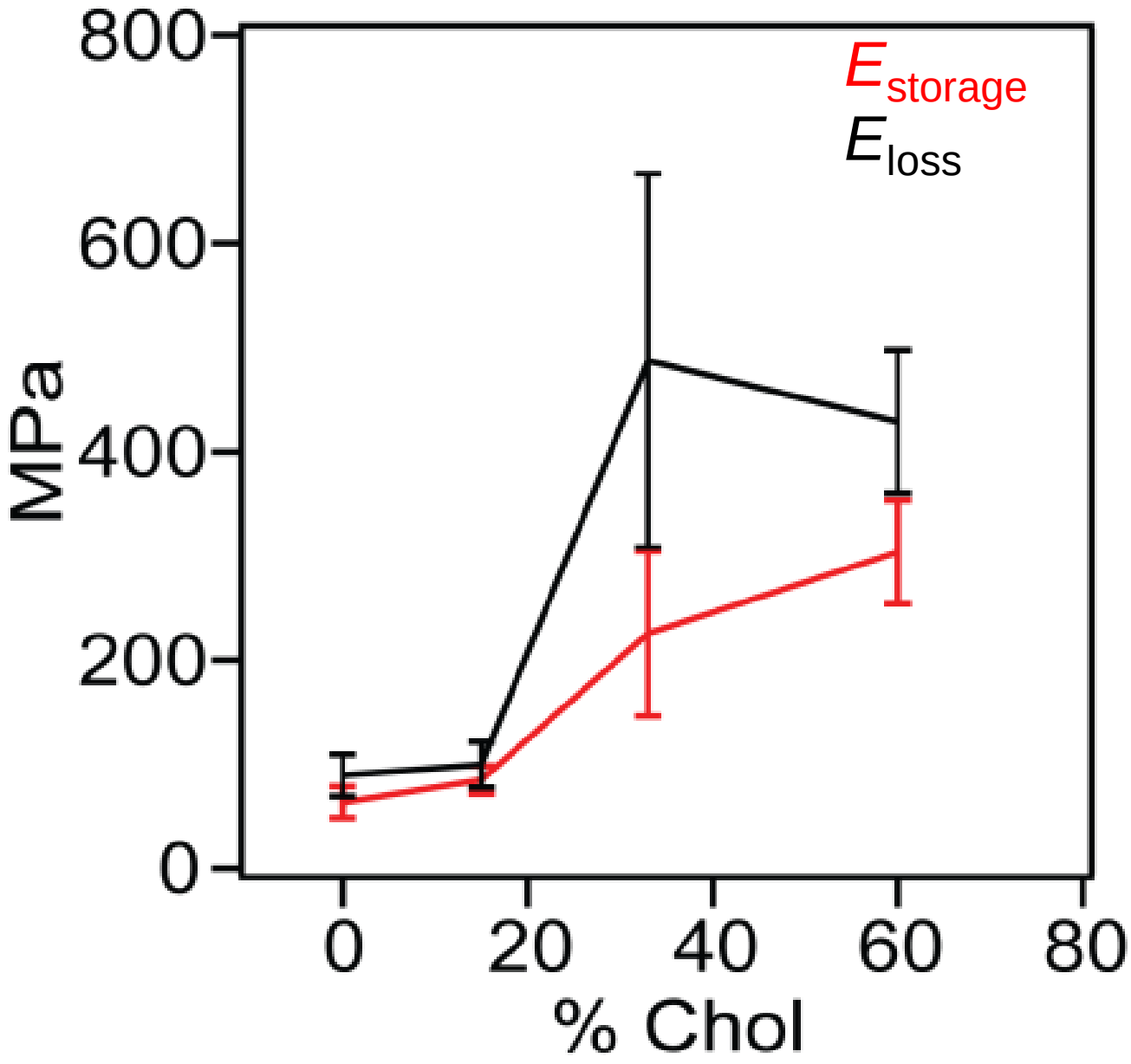
800
600
400
200
0
MPa
0
20
40
60
80
% Chol
E storage
E loss

Supporting Information

SI Materials and Methods

Supported lipid bilayers (SLB). SLBs were obtained through the commonly used method, small unilamellar vesicle fusion (1). Circular mica surfaces (Ted Pella, Redding, CA, USA) were used as SLB substrates for the experiments. Initially, mica surfaces were mounted onto metal discs using high-vacuum silicone grease (Dow Corning, Midland, MI, USA). Freshly cleaved mica supports were initially lubricated with 100 ml of 20 mM NaCl. This was followed by placing 7 µl of SUV suspension onto the mica and allowing them to settle at room temperature for 20 min. Next, the samples were rinsed several times with 20 mM NaCl to avoid unfused vesicles, but were always kept hydrated. The samples were then heated to 60◦C for 45 mins. The SLB preparation process is shown in Fig. 1B.

AM-FM AFM. After slowly cooling down the sample, it was mounted onto the Asylum Research Cypher AFM (Oxford Instruments Asylum Research, Santa Barbara, USA) and imaged. Using AM-FM mode, two separate excitation signals were combined to excite two cantilever resonances simultaneously. The principle of AM-FM operation in aqueous environment has been previously described (2-5). Briefly, the first resonance was monitored in standard tapping mode (AM mode), providing the topography through feedback on the first-resonance amplitude, (Fig. 1C). Meanwhile, the cantilever was driven to oscillate at a second resonance, where the frequency was tracked by the controller (FM mode), (Fig. 1C). This implied that a stiffer sample will shift the oscillation of the higher normal mode to a higher frequency (6-8). Since, AM-FM AFM involves the excitation of two cantilever eigenmodes (3, 4), we can therefore measure the deflection of cantilever as $z(t) = z_0 + A_2\cos(\omega_2 t - \varphi_2) + A_3\cos(\omega_3 t - \varphi_3) + O(\alpha)$, where z_0 is the mean deflection and $O(\alpha)$ contains higher order terms, which are usually very small. The amplitude of the second eigenmode (A_2) is used to track the topography of the material, while the amplitude and phase of the third eigenmode are used to map both the conservative and dissipative components of the tip-sample interaction (3, 4, 9). In brief, the bimodal excitation and detection with FM mode of the AFM under aqueous conditions, provides simultaneous information on both topography and local elastic modulus (storage), (3, 4). Furthermore, the signal of the lower frequency is used to establish the feedback mechanism as in regular FM AFM while the higher frequency is sampled to provide the elastic modulus. Therefore, in AM-FM AFM quantitative information of materials are extracted from the projection of the continuous beam deflection over the cantilever eigenmodes. Applying both energy conservation and the virial theorem to the third eigenmode (free) gives two independent equations:

$E_3^{dissipated} = -\int_0^T F_{tip-sample}(d) \cdot \dot{z}_3(t)dt = \frac{\pi k_3 A_3}{Q_3} (A_{0,3} sin\varphi_3 - A_3)$ and $V_3^{tip-sample} = \frac{1}{T}\int_0^T F_{tip-sample}(d) \cdot z_3(t)dt = -\frac{k_3 A_{0,3}}{2Q_3} A_3 cos\varphi_3$, where $E^{dissipated}$ is the energy dissipated by the tip-sample forces, $V_{tip-sample}$ is the virial tip-sample forces and $F_{tip-sample}$ is the tip-sample forces. The virial equation can be simplified using previous approximations (10) to express a relationship between the gradient of the interaction forces and phase shift of the third mode to give, $F'_{tip-sample}(d) \approx C \frac{k_3 A_{0,3}}{A_3(z_c) Q_3} cos\varphi_3(z_c)$, where $A_{0,3}$, k_3 and Q_3 are the free amplitude, spring constant and quality factor of the third eigenmode respectively. There is a correction factor, C that converges for high ratios ($A_{0,2}/A_{0,3}$) and finally, the relevant distances in the theory used for the tip-sample separation is $d = z + z_c = z_c - A_2 - A_3$. Using the Hertz contact model for a paraboloid indenter of radius R , the elasticity of the sample is related to the tip-sample stiffness by the relation $k_{int}(\delta) = 2E\sqrt{R\delta}$, where E is the elastic modulus (storage modulus) and δ is the indentation depth. Therefore, a relationship between φ_3 and E can be obtained where $F'_{tip-sample}(z_c) = 2E\sqrt{R\delta} = 2Er_c$, where r_c is the true contact radius, which has been derived in detail elsewhere (5). In the FM mode, the elastic modulus maps ($E_{storage}$) are determined by recording $A_3(x, y)$ and $\varphi_3(x, y)$ and hence we can determine those maps from the above equations, where $E = \frac{1}{2r_c} \frac{k_3 A_{0,3}}{A_3(z_c) Q_3} cos\varphi_3(z_c)$. Consequently, as described elsewhere in detail (8, 11), a loss tangent map is obtained from the amplitude and phase signals in the AM mode. Since this technique is based on the Kelvin-Voigt viscoelastic model, we know that the loss tangent is equivalent to the ratio of the dissipated energy to stored energy ($\tan\delta = E_{loss}/E_{storage}$), allowing us to obtain the loss modulus ($E_{loss} = E_{storage} \tan\delta$). In this study, AM-FM AFM was used to estimate the $E_{storage}$ and E_{loss} of DPPC:Chol (0-60%) lipid bilayers. We used OMCL-RC800PSA silicon nitride tips with a spring constant of 0.76 N/m (Olympus, Tokyo, Japan). Cantilevers were calibrated using the Sader method (12). The tip was brought in contact with the sample and the drive frequency was carefully adjusted to the resonant frequency of the second normal mode of vibration of the cantilever (f_2 ~ 150 kHz) with a larger free amplitude at (~ 50 – 100 nm). Meanwhile, the cantilever was driven at a second resonance, characterized by higher frequency (f_3 ~ 420 kHz), corresponding to the third normal mode with much smaller amplitude (~ 0.5 – 2 nm). The third mode was adjusted to keep the phase at 90° on resonance. After the method was calibrated using a sample of known elastic modulus (DPPC), the tip was retracted, and the calibration sample was replaced by the sample of interest. When the tip-to-surface approach was completed, both resonances were tuned again. The drive set-point of the second normal mode was 700-800 mV and that of the higher mode was 20 mV. A low

A_3/A_0 ensured optimal tracking of the surface topography, which was important to obtain proper results in AM-FM AFM. All results in this work are freely available from our lab by contacting the corresponding authors.

Data deposition: All results in this work have been deposited in figshare (https://figshare.com/articles/PNAS_paper_zip/5894584).

Data analysis. The images were rendered and post-processed with the software IGOR PRO 6.2 (WaveMetrics, Lake Oswego, OR, USA). Post-processing included cropping and flattening the images using the 1st, 3rd or histogram flatten order. In this study, $E_{storage}$ and E_{loss} of mixtures of DPPC, DPPC:Chol (15%), DPPC:Chol (33%) and DPPC:Chol (60%) were obtained using IGOR. Histograms were plotted for the distribution of the moduli recorded for all pixels of the image. The histograms were fitted with gaussian fits in Matlab (The MathWorks, Natick, MA, USA), providing both the mean and standard deviation (SD), (Table S1). All results presented in this work are freely available from our lab by contacting the corresponding authors. Data deposition: All results in this work have been deposited in figshare (https://figshare.com/articles/PNAS_paper_zip/5894584).

References

1. Mingeot-Leclercq MP, Deleu M, Brasseur R, & Dufrene YF (2008) Atomic force microscopy of supported lipid bilayers. *Nat Protoc* 3(10):1654-1659.
2. Kocun M, Labuda A, Meinhold W, Revenko I, & Proksch R (2017) Fast, High Resolution, and Wide Modulus Range Nanomechanical Maping with Bimodal Tapping Mode. *ACS Nano DOI: 10.1021/acsnano.7b04530.*
3. Garcia R & Proksch R (2013) Nanomechanical mapping of soft matter by bimodal force microscopy. *Eur Polym J* 49(8):1897-1906.
4. Martinez-Martin D, Herruzo ET, Dietz C, Gomez-Herrero J, & Garcia R (2011) Noninvasive Protein Structural Flexibility Mapping by Bimodal Dynamic Force Microscopy. *Phys Rev Lett* 106(19):198101.
5. Labuda A, Kocun M, Meinhold W, Walters D, & Proksch R (2016) Generalized Hertz model for bimodal nanomechanical mapping. *Beilstein J Nanotechnol* 7:970-982.
6. Guo S, *et al.* (2012) Multifrequency imaging in the intermittent contact mode of atomic force microscopy: beyond phase imaging. *Small* 8(8):1264-1269.

7. Solares SD & Chawla G (2010) Triple-frequency intermittent contact atomic force microscopy characterization: Simultaneous topographical, phase, and frequency shift contrast in ambient air. *J Appl Phys* 108(5):054901.
8. Proksch R & Yablon DG (2012) Loss tangent imaging: Theory and simulations of repulsive-mode tapping atomic force microscopy. *Appl Phys Lett* 100(7):073106.
9. Lozano JR & Garcia R (2008) Theory of multifrequency atomic force microscopy. *Physical review letters* 100(7):076102.
10. Kawai S, *et al.* (2009) Systematic achievement of improved atomic-scale contrast via bimodal dynamic force microscopy. *Phys Rev Lett* 103(22):220801.
11. Proksch R, *et al.* (2016) Practical loss tangent imaging with amplitude-modulated atomic force microscopy. *J Appl Phys* 119(13):134901.
12. Sader JE, Chon JWM, & Mulvaney P (1999) Calibration of rectangular atomic force microscope cantilevers. *Rev Sci Instrum* 70(10):3967-3969.

Supplemental Information Legends

Fig. S1 The frequency modulation (FM) component of AM-FM AFM. The second resonance provides the amplitude (A_3) and frequency (f_3) information of DPPC:Chol with various molar fractions of Chol: (A) DPPC (0 mol %; scan size: 3.5 µm); (B) 15 mol % (scan size: 5.2 µm), which appears darker than the substrate, suggesting that the material is softer than the background; (C) Both 33 mol % (scan size: 5.4 µm); and (D) 60 mol % (scan size: 3.8 µm) appear homogenous. Scale bar: 500 nm (bottom left-hand corner).

Fig. S2 Loss tangent values as function of molar fractions of Chol. The tanδ values for each respective mol % of Chol in the DPPC:Chol model system.

Fig. S3 Storage and loss moduli as a function of loss tangent values. The mean E_{storage} (red) and E_{loss} (black) of the DPPC:Chol as function of the loss tangent values (tanδ). The error bars correspond to the SD.

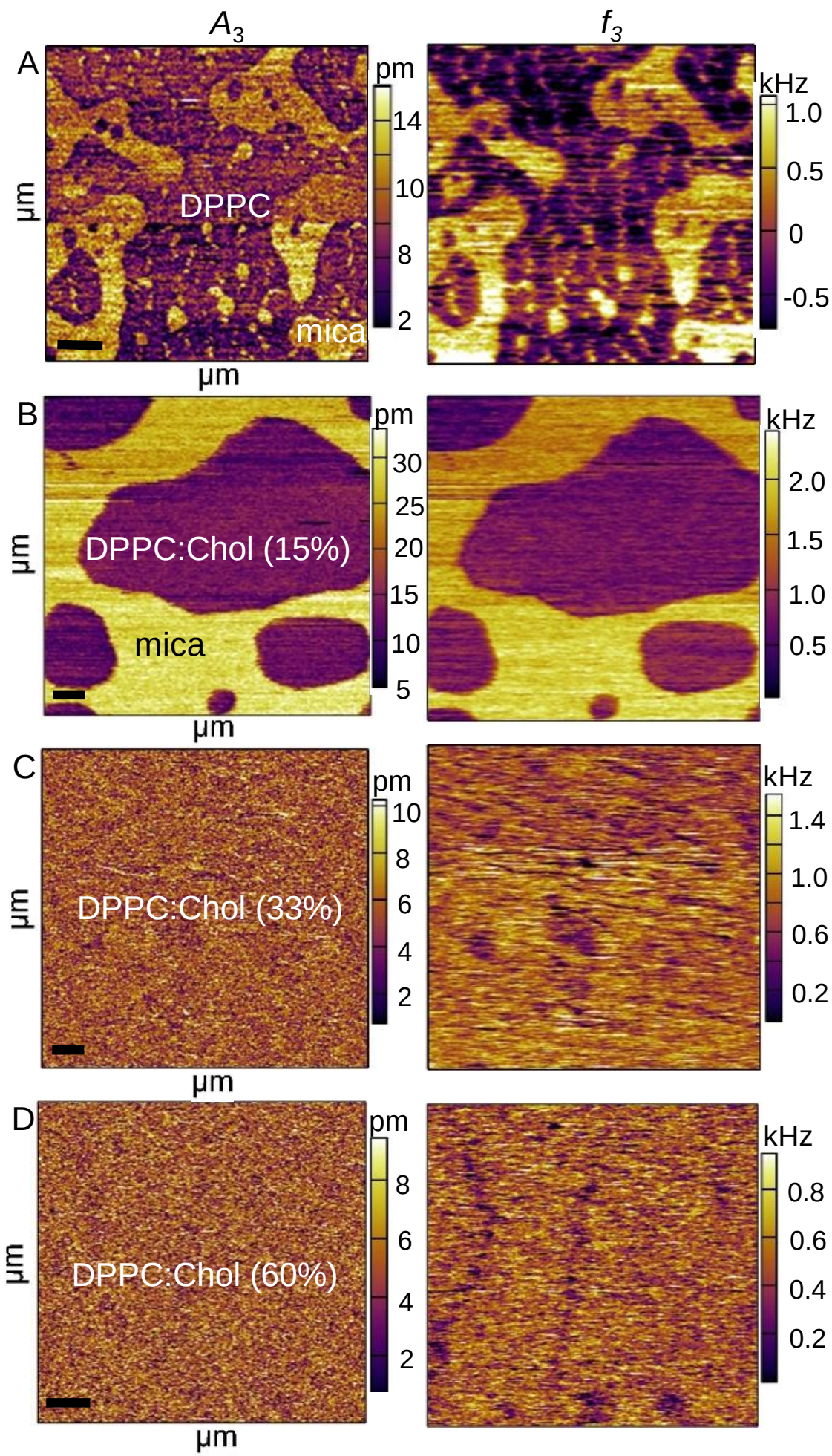
A_3
f_3
A
DPPC
mica
µm
pm
14
10
8
2
kHz
1.0
0.5
0
-0.5
B
DPPC:Chol (15%)
mica
µm
pm
30
25
20
15
10
5
kHz
2.0
1.5
1.0
0.5
C
DPPC:Chol (33%)
µm
pm
10
8
6
4
2
kHz
1.4
1.0
0.6
0.2
D
DPPC:Chol (60%)
µm
pm
8
6
4
2
kHz
0.8
0.6
0.4
0.2

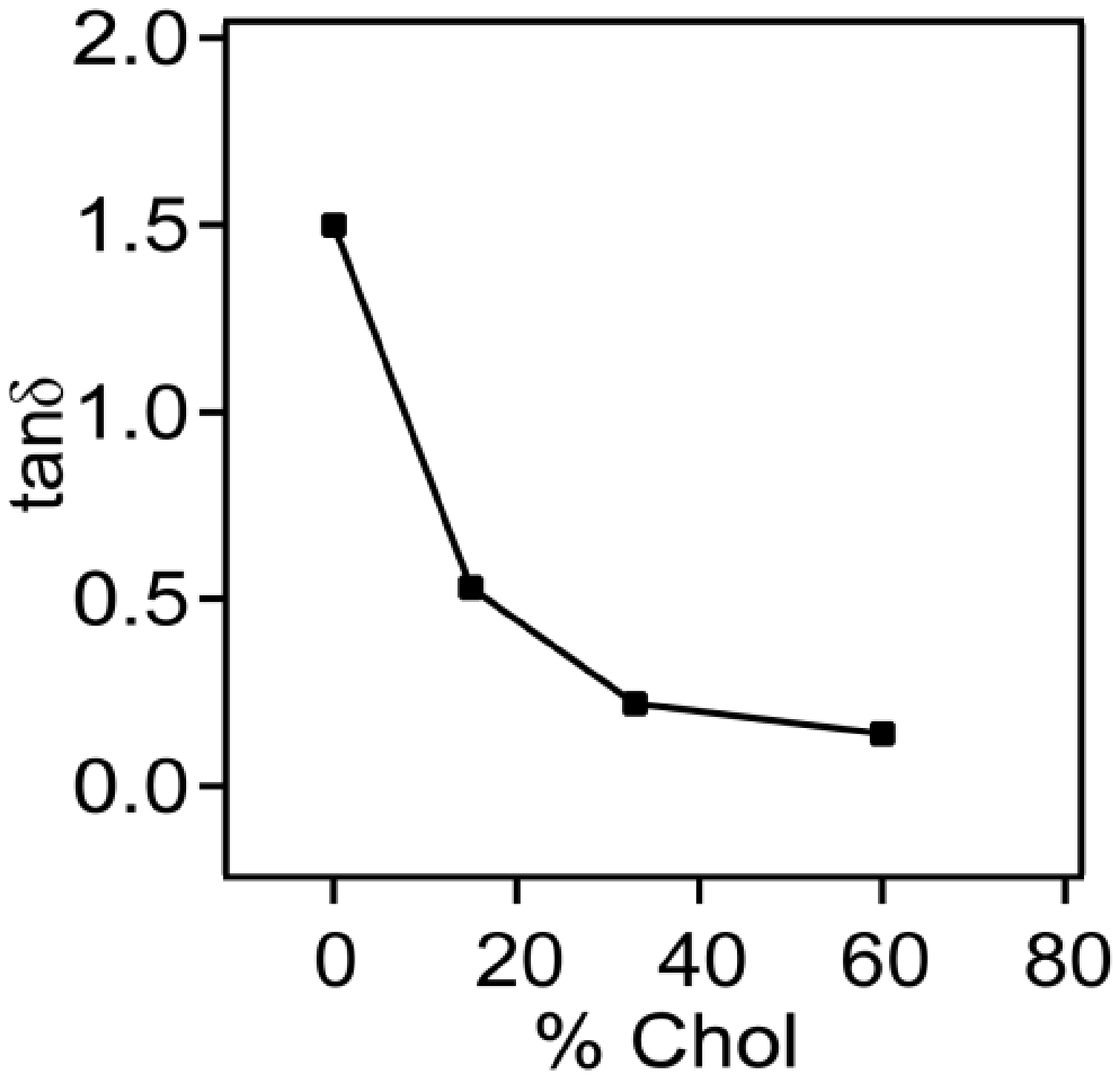
2.0
1.5
1.0
0.5
0.0
tanδ
0
20
40
60
80
% Chol

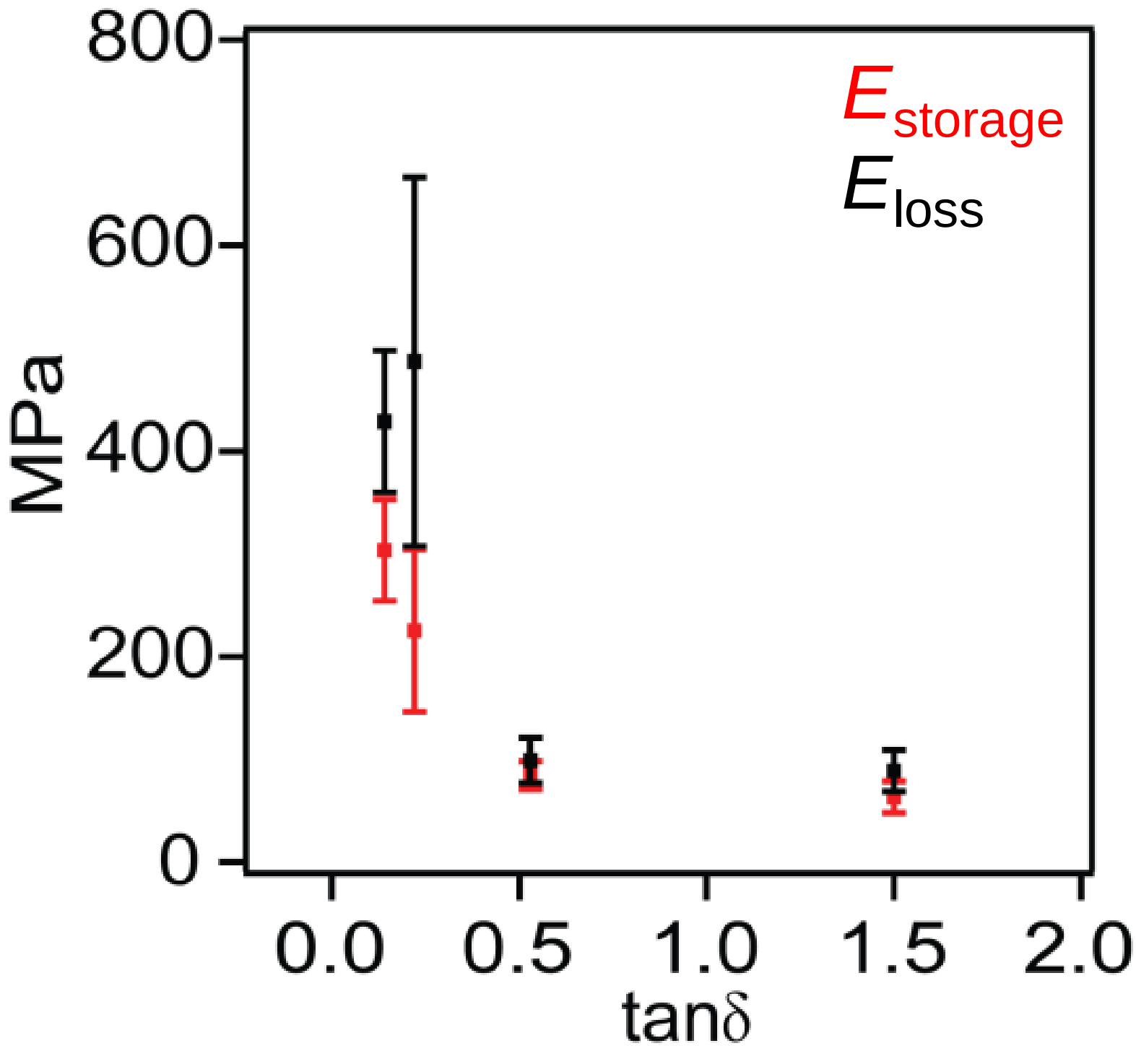
800
600
400
200
0
MPa
$E_{storage}$
E_{loss}
0.0
0.5
1.0
1.5
2.0
tanδ

Table S1. Storage and loss moduli of DPPC:Chol mixtures.

DPPC:Chol Mixtures	$E_{storage}$ (MPa)	E_{loss} (MPa)
DPPC	63.3 ± 15.3	89.0 ± 20.0
DPPC:Chol (15%)	84.8 ± 13.5	99.2 ± 22.0
DPPC:Chol (33%)	225 ± 79.2	487 ± 179
DPPC:Chol (60%)	304 ± 49.4	429 ± 68.9